

Portable standoff spectrometer for hazard identification using integrated quantum cascade laser arrays from 6.5 to 11 μm .

MARK F. WITINSKI,^{1,*} ROMAIN BLANCHARD,¹ CHRISTIAN PFLUEGL,¹ LAURENT DIEHL,¹ BIAO LI,¹ KALYANI KRISHNAMURTHY,¹ BRANDT C. PEIN,¹ MASUD AZIMI,¹ PEILI CHEN,¹ GOKHAN ULU,¹ GREG VANDER RHODES,¹ CHRIS R. HOWLE,² LINDA LEE,² RHEA J. CLEWES,² BARRY WILLIAMS,³ AND DARYOOSH VAKHSHOORI,¹

¹*Pendar Technologies, 30 Spinelli Place, Cambridge, MA 02138, USA*

²*Dstl, Porton Down, Salisbury, SP4 0JQ, UK*

³*Leidos, PO Box 68, Gunpowder, MD 21010-0068, USA*

*witinski@pendar.com

Abstract: This article presents new spectroscopic results in standoff chemical detection that are enabled by monolithic arrays of Distributed Feedback (DFB) Quantum Cascade Lasers (QCLs), with each array element at a slightly different wavelength than its neighbor. The standoff analysis of analyte/substrate pairs requires a laser source with characteristics offered uniquely by a QCL Array. This is particularly true for time-evolving liquid chemical warfare agent (CWA) analysis. In addition to describing the QCL array source developed for long wave infrared coverage, a description of an integrated prototype standoff detection system is provided. Experimental standoff detection results using the man-portable system for droplet examination from 1.3 meters are presented using the CWAs VX and T-mustard as test cases. Finally, we consider three significant challenges to working with droplets and liquid films in standoff spectroscopy: substrate uptake of the analyte, time-dependent droplet spread of the analyte, and variable substrate contributions to retrieved signals.

© 2018 Optical Society of America under the terms of the [OSA Open Access Publishing Agreement](#)

OCIS codes: (300.6340) Spectroscopy, infrared; (140.5965) Semiconductor lasers, quantum cascade; (280.3420) Laser sensors; (300.6360) Spectroscopy, laser.

References and links

1. S. Wallin, A. Pettersson, H. Östmark, and A. Hobro, "Laser-based standoff detection of explosives: a critical review," *Anal. Bioanal. Chem.* **395**(2), 259–274 (2009).
2. M. Gaft and L. Nagli, "Standoff laser-based spectroscopy for explosives detection," in G. W. Kamerman, O. K. Steinvall, K. L. Lewis, K. A. Krapels, J. C. Carrano, and A. Zukauskas, eds. (International Society for Optics and Photonics, 2007), Vol. **6739**, p. 673903.
3. B. Hinkov, F. Fuchs, J. M. Kaster, Q. Yang, W. Bronner, R. Aidam, and K. Köhler, "Broad band tunable quantum cascade lasers for stand-off detection of explosives," in J. C. Carrano and C. J. Collins, eds. (International Society for Optics and Photonics, 2009), Vol. **7484**, p. 748406.
4. P. M. Pellegrino, E. L. Holthoff, and M. E. Farrell, *Laser-Based Optical Detection of Explosives* (CRC Press, 2017).
5. J.-M. Thériault, E. Puckrin, J. Hancock, P. Lecavalier, C. J. Lepage, and J. O. Jensen, "Passive standoff detection of chemical warfare agents on surfaces," *Appl. Opt.* **43**(31), 5870–5885 (2004).
6. B. G. Lee, J. Kansky, A. K. Goyal, C. Pflügl, L. Diehl, M. A. Belkin, A. Sanchez, and F. A. Capasso, "Beam combining of quantum cascade laser arrays," *Opt. Express* **17**(18), 16216–16224 (2009).
7. B. G. Lee, M. A. Belkin, C. Pflügl, L. Diehl, H. A. Zhang, R. M. Audet, J. MacArthur, D. P. Bour, S. W. Corzine, G. E. Huffer, and F. Capasso, "DFB Quantum Cascade Laser Arrays," *IEEE J. Quantum Electron.* **45**(5), 554–565 (2009).
8. L. Diehl, B. G. Lee, H. A. Zhang, C. Pflügl, M. Belkin, M. Fisher, A. Wittman, J. Faist, and F. Capasso, "Broadband Distributed Feedback Quantum Cascade Laser Array Using a Heterogeneous Cascade," in *Conference on Lasers and Electro-Optics/International Quantum Electronics Conference* (OSA, 2009), p. CThT1.
9. K. Degreif, S. Rademacher, P. Dasheva, F. Fuchs, S. Hugger, F. Schnürer, and W. Schweikert, "Stand-off explosive detection on surfaces using multispectral MIR-imaging," in M. Ramezani, R. Sudharsanan, and G. J.

- Brown, eds. (2011), p. 79450P.
10. F. Fuchs, "Imaging standoff detection of explosives using widely tunable midinfrared quantum cascade lasers," *Opt. Eng.* **49**(11), 111127 (2010).
 11. G. Ouyang, M. N. Akram, K. Wang, Z. Tong, and X. Y. Chen, "Laser speckle reduction based on angular diversity induced by Piezoelectric Benders," *J. Eur. Opt. Soc.* **8**, 13025 (2013).
 12. I. Freund, "Joseph W. Goodman: Speckle Phenomena in Optics: Theory and Applications," *J. Stat. Phys.* **130**(2), 413–414 (2007).
 13. M. B. Mitchell, "Fundamentals and Applications of Diffuse Reflectance Infrared Fourier Transform (DRIFT) Spectroscopy," *Adv. Chem.* **236**, 351–375 (1993).
 14. T. Armaroli, T. Bécue, and S. Gautier, "Diffuse Reflection Infrared Spectroscopy (Drifts): Application to the in Situ Analysis of Catalysts," *Oil Gas Sci. Technol.* **59**(2), 215–237 (2004).
 15. R. Harig, R. Braun, C. Dyer, C. Howle, and B. Truscott, "Short-range remote detection of liquid surface contamination by active imaging Fourier transform spectrometry," *Opt. Express* **16**(8), 5708–5714 (2008).

1. Introduction

Identifying chemical residues in a standoff situation can mitigate potential hazards in suspected cases of CWA or explosives contamination. This has spurred development of commercial long wave infrared (LWIR) standoff detection systems that analyze the reflectance from chemical/substrate backscattering in both passive and active illumination modes [1–4]. The LWIR spectral region is particularly important for such interrogation since most condensed phase materials exhibit both unique and intense spectral features related to molecular vibrational modes in this portion of the electromagnetic spectrum. The numerous challenges of reliable standoff detection analysis stem from the plethora of possible chemical/substrate presentations and scales of time-evolution particularly in the case of liquid-phase chemicals which can evaporate, spread across a surface or diffuse into the substrate. Addressing these challenges requires parallel advances in several areas of expertise including: cutting-edge laser packaging and optical design, integrated laser electronics, statistically robust decision algorithms, and deep chemical knowledge. In this work we describe a portable detector that addresses each of these challenges and demonstrate its efficacy in identifying two CWAs, VX and T-mustard, presented on multiple substrates at a standoff distance of 1.3 meters.

The development of a practical instrument capable of identification against a large library of chemicals requires widely tunable LWIR sources that are rugged enough to be deployable. This is because (1) the linewidths of absorption features can be broad, particularly for the condensed phase, and (2) vibrational modes from multiple chemical targets tend to overlap intermittently throughout the LWIR, also known as the spectral fingerprint region (ca. 500 – 1500 cm^{-1}). Suitable algorithmic confidence and elimination of false positives therefore requires adequate wavelength coverage. In addition to broadband tunability, the laser source must quickly scan its emission wavelength while maintaining high reproducibility in power and wavelength, allowing for efficient signal averaging through multiple measurements. This is especially important for the standoff detection of chemicals in handheld systems where available averaging time is often short due, for example, to hand movements and aiming drift when training a laser beam onto a small target of sample from distances exceeding one meter. To achieve broadband tunability and measurement speed we have developed a monolithic LWIR light source consisting of four 32-element DFB QCL arrays (QCLAs) that cover a spectral region between 6.5 and 10.5 μm .

2. Sensor Design and Test

2.1. Light Source: Quantum Cascade Laser Arrays

The wavelength region between 6.5 – 10.5 μm (1540 – 950 cm^{-1}) is ideal for sensitive and specific detection of explosives, CWAs [5], and other hazardous materials because the region generally encompasses the most strongly absorbing features within those molecules. At the core of the present approach to producing such breadth in that region is the DFB QCLA [6–8]. First developed by Capasso and associates, the near-continuously tunable QCLA source is

fully monolithic and offers significant advantages compared to other broadband tunable sources, such as External Cavity QCLs. The distinct advantages of QCLAs are especially germane for field or handheld applications, where speed, ruggedness, and stability are paramount. Specifically, QCLAs are favorable because of: (1) their monolithic structure underpinning inherent ruggedness and production scalability, (2) their fully electronic wavelength tuning, allowing for high speed tuning, and (3) high amplitude and wavelength stability, which is critical for the rapid signal averaging that standoff examination demands. An Allan deviation plot for a typical element of a QCLA combined with an uncooled HgCdTe (MCT) detector is shown in Fig. 1. This Allan deviation plot indicates that for this system, the most reproducible measurement is obtained with 20,000 laser pulses. It should be noted that the noise shown here is not necessarily limited by the pulse-pulse noise of the QCLA element but rather the combination of the laser and the MCT detector, as well as the data acquisition electronics. As we will discuss below, a single LWIR spectrum requires 294.4 μ s so, in accordance with the Allan deviation plot, a reliable spectrum can be collected in < 5 seconds, a timescale useful for the cases of time-evolving residue interrogation.

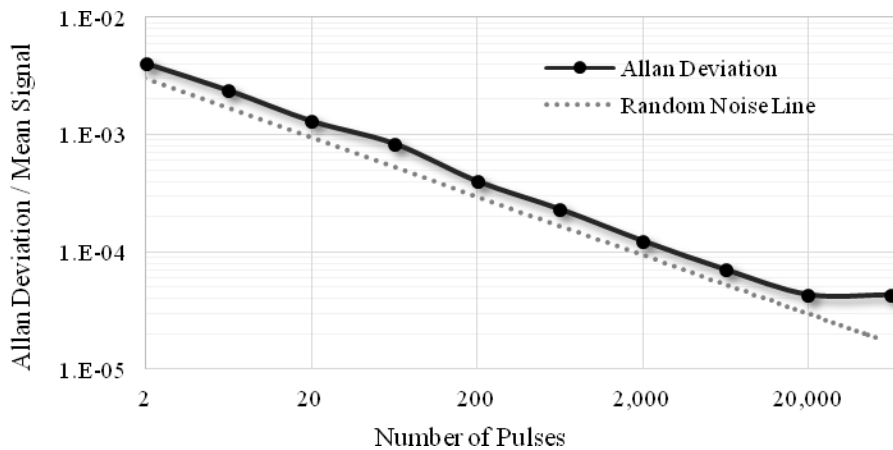


Fig. 1. Allan deviation plot for a typical element of a QCLA. The data is obtained by acquiring the time trace of the laser pulses with an uncooled MCT detector (1 mm x 1 mm) located directly in front of the diverging laser beam. The distance between the laser and the detector was set to obtain a signal that was one third of the saturation signal of the detector. The signal output was amplified, low-passed at 20MHz, and digitized at 125 MS/s with 12-bits vertical resolution. The measurement for each pulse is defined as the integrated signal over a full pulse. Note that these values represent a high bound of the QCLA noise, and that the noise characterization setup used here is limited by the dynamic range of the detector as well as timing jitter between the laser pulse driver and the analog to digital converter.

Additionally, there are a few less obvious aspects to these sources that make them well suited to support portable spectroscopy methods. For one, the laser array can maintain a 100% *aggregate* duty cycle while each laser in the array requires operation only over a $100/n$ (%) duty cycle, where n is the number of lasers in the array. Put another way, a laser array consisting of only pulsed QCLs can illuminate as a continuous-wave (CW) system does, allowing for high measurement duty cycle, while reducing the cost of fabrication and significantly increasing the wall-plug efficiency. Another advantage of QCLA technology is the arbitrary programmability of which wavelengths are delivered and when, a trade-space that would open many new possibilities for experimental optimization across a range of different applications. Certain lasers can be skipped, multiple lasers can fire at once, pulse repetition rates and durations can be set for each element, and so on. In particular, this has potential applications for high speed multi-spectral imaging [9].

For the present work, four 32-element QCLAs were fabricated, each array covering a distinct band of the LWIR, resulting in a combined coverage of $6.5 - 10.5 \mu\text{m}$. The four bands were spectrally beam combined, using dielectric mirrors and polarization techniques, forming a package (hereafter light engine) which measures $8 \text{ cm} \times 8 \text{ cm} \times 1.5 \text{ cm}$.

2.2 Laser Integration

The standoff spectrometer used for this work was built around the light engine described in Section 2.1. Similar QCL-based systems have been described elsewhere [10]. Figure 2 shows the block diagram of the spectrometer, along with a photograph.

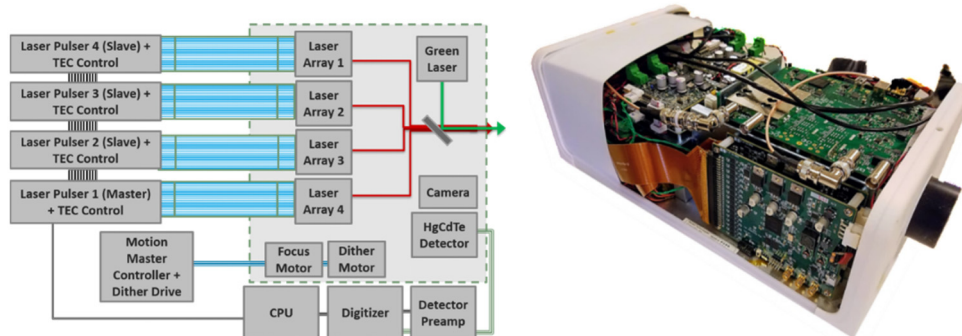


Fig. 2. (left) Block Diagram of spectrometer showing optical and electronic components and their interconnects. (right) An integrated system based on the 4-array laser and commercially available circuits for \ operation and high-speed data acquisition. It weighs 8 kg and measures $35 \text{ cm} \times 22 \text{ cm} \times 12 \text{ cm}$ in $L \times W \times H$, respectively.

The lasers were operated in pulsed mode and focused to a spot size of 2 mm onto the targets. Randomly dithering the combined beam's pointing angle slightly ($\sim 1^\circ$ full angle) was helpful to mitigate speckle [11,12], resulting in a square profile of $\sim 2 \text{ cm}$ /side at a standoff distance of 1.3 m. This is illustrated in Fig. 3, which shows IR images (Seek Thermal) of the interrogation beam at 1.3 m with dither off and with dither on. The dither off image is useful in confirming that the outputs of the four arrays are indeed beam-combined and focused to a spot size of $\sim 2 \text{ mm}$. Turning on the dither moves the combined illumination over $2 \text{ cm} \times 2 \text{ cm}$. The dither area size is approximately 60×60 diffraction limited spots at $10 \mu\text{m}$ wavelength with a 2" aperture, corresponding to an expected speckle reduction by a factor of ~ 60 . As discussed later, while dither reduces speckle, it may not always provide the highest data quality, especially when the signal is dominated by specular reflection off a smooth surface (e.g. glass, air/liquid interface).

The sequence of laser firing used for the present work was as follows: A 300 ns pulse was applied sequentially to each of the 128 lasers, and the firing order was interleaved between arrays [i.e. (laser 1, array 1), (laser 1, array 2), (laser 1, array 3), (laser 1, array 4), (laser 2, array 1), ...] to reduce the risk of thermal cross-talk between neighboring lasers on the same array. Due to a limitation of the electronics used in this prototype, a $2 \mu\text{s}$ delay between adjacent laser channels was necessary such that a single LWIR scan required $294.4 \mu\text{s}$. A scan duty cycle of 50% was used, resulting in a scan repetition period of $589 \mu\text{s}$ and an overall measurement duty cycle of 6.5%. In the data presented later, 5,625 of these nominally identical scans were averaged, such that a data acquisition time of 3.3 seconds was used as standard.

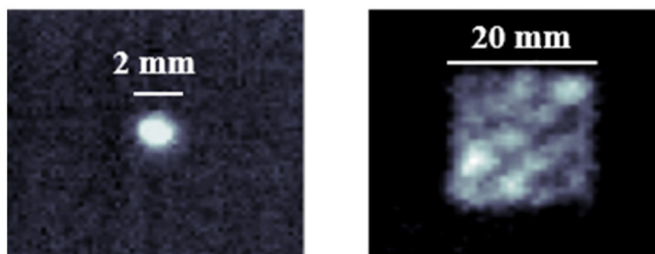


Fig. 3. Infrared images of the dithered and non-dithered beams. Images were obtained 1.3 m from the instrument.

2.3 Baseline Instrument Testing

Before considering the challenges presented by liquid droplets of VX and T-mustard, baseline performance characterization of the new spectrometer was performed using bulk finely ground powders. The most suitable data for performance evaluation of the sensor are obtained using Diffuse Reflectance Infrared Fourier Transform Spectroscopy (DRIFTS), since this method most closely reproduces the standoff instrument measurement modality being diffuse reflectance spectroscopy (DRS). These techniques are well described elsewhere [13,14]. Pendar has built a custom DRIFTS setup for evaluating the standoff instrument's data quality. The data presented in this section compare the spectra of the QCLA-based sensor with those obtained using DRIFTS. Both the standoff and DRIFTS data were acquired using the same test samples and substrates on the same day. Typical performance for various bulk powders are presented along with DRIFTS spectra in Fig. 4. The spectra in Fig. 4 consist of 5,625 coadded spectra, requiring 3.3 seconds to obtain at a standoff distance of 1.3 meters.

All standoff instrument DRS data reported in the following sections use the term 'Normalized Reflectance' on the y-ordinate axis. Here, normalization refers to the background differential scatter from a sandblasted aluminum coupon. Other than coadditions of successive spectra, no additional data treatment was performed on any of the experimental DRS data.

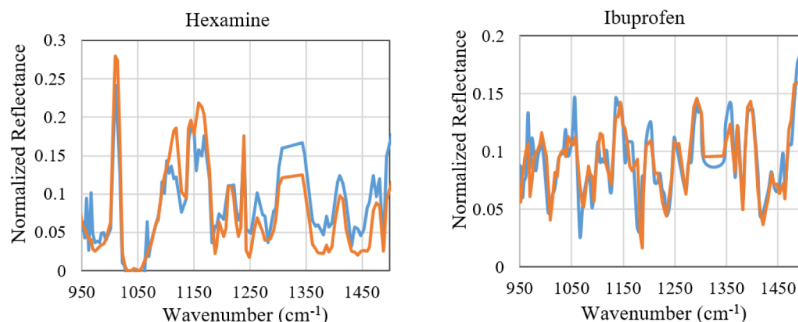


Fig. 4. Two representative comparisons between the DRS-based spectrometer scans of bulk powders (blue) and the DRIFTS spectra of same samples (orange).

Having demonstrated agreement between standoff DRS and DRIFTS for bulk powders, the standoff instrument was then tested against more challenging chemical presentations – single droplets of chemical hazard contamination on a host of substrates.

2.4 Testing of VX and T-Mustard

Experiments using these extremely hazardous liquid CWAs were carried out at the Defence Science and Technology Laboratory (Dstl) in the UK. All samples and substrates were handled by agent handlers in a fume cupboard and incinerated after use. A folding mirror was

placed inside of the fume cupboard to direct the illumination and scatter onto and from test coupons that were lying flat in a fume cupboard, allowing the spectrometer to be placed approximately 1 m away from the sash, resulting in a pathlength from output to sample of 1.3 meters. Two cameras were focused onto the sample stage: a visible camera for capturing images and video as well as an IR camera (SEEK Thermal). The IR camera was used to ensure co-alignment of the QCLA interrogation beam with the green sighting laser, an alignment that was periodically confirmed by turning off the dither and overlaying the two.

Deposition of VX (CAS # 50782-69-9) and T-mustard (CAS # 63918-89-8) was performed, using micropipettes, on multiple substrates including dry sand (Arcos, 40 – 150 mesh, ca. 0.42 – 0.105 mm), borosilicate glass slides, and bead-blasted stainless steel. All agents were deposited neat and with a purity > 87% as analyzed by NMR and GC-MS methods.

2.5 Spectroscopic signature analysis

The spectral signatures measured can feature aspects of the limiting cases listed below, depending especially on the analyte morphology (e.g. droplet size and shape, film thickness, air/analyte interface roughness), the analyte and substrate complex refractive indices and the angle of incidence of the probe laser beam. These parameters are in turn affected by chemical and physical characteristics of the analyte and substrate: for example, a droplet shape is influenced by the surface tension and viscosity of the analyte as well as its substrate affinity.

- *Absorption-dominated signature:* Samples that favor strong penetration into the analyte may have signatures dominated by the absorption coefficient (α) of the analyte and will tend to be governed by Beer's Law:

$$A = \alpha CL \quad (1)$$

The absorptivity coefficient is similar in appearance to the imaginary part of the refractive index (k), and in this case, the DRS spectrum will more closely match k .

- *Air/Analyte Fresnel reflection-dominated signature:* Some samples where the air/analyte interface is smooth and specular reflection is captured by the receiver, may present a DRS spectral signature that more closely corresponds to the Fresnel reflection. The equation below describes the resulting reflection spectrum when the sample is interrogated at a near-normal angle of incidence:

$$R = \frac{(n-1)^2 + k^2}{(n+1)^2 + k^2} \quad (2)$$

Knowledge of the two parts of the complex refractive index n and k thus allows one to calculate the corresponding reflection spectrum.

- *Substrate interference:* The dither of our probe beam is implemented to reduce, by spatial averaging, the effect of the speckle originating from reflection off a rough sample. However, if the analyte is smaller than the dither area (of 20 mm × 20 mm), the integrated response measured will be the sum of the contributions obtained when the beam is on the analyte (often probing both analyte and substrate) and when the beam is on the substrate (probing only the substrate's diffuse reflectance). Even in the case of a homogeneous sample over the area of beam dithering, the substrate signature can manifest itself, depending for example on the thickness of the analyte, its absorbance, or the morphology of the interfaces involved

Actual measurements often convolve a mixture of these reflection profiles. The morphology of the analyte may change over time as it evaporates or spreads out on or soaks into the substrate. The resulting spectra may, therefore, transition between reflection and

absorption-dominated modes, as discussed in more detail in the next section. The rather simple models shown above are used at this point mostly as guides to understand the spectral signatures observed, and not as predictive models, although these limiting cases do highlight the importance of knowing both the real and imaginary part of the complex refractive index (n and k , respectively) to interpret the scattering data obtained.

3. Droplet Testing of VX and T-mustard

The central challenges introduced by droplet examination compared to bulk or residual powders rest on top of the significant challenges of DRS generally. Among these, we consider: (1) seepage of the liquid into a porous substrate (2) time dependent morphology as the hemispheric droplets often spread into a thin film, the rate of which depends on the surface tension of the analyte itself as well as its contact angle and liquid viscosity, neither of which is generally known *a priori*, and (3) the hemispheric nature of droplets, where slight changes in alignment can suppress specular contributions with respect to absorptive ones. The following three sections examine VX and T-mustard data in these three contexts.

3.1. Absorption Into substrate

With the sand coupon placed at the center of the interrogation beam, six 10- μL droplets of VX were dispensed a few millimeters apart from one another. The DRS spectrum of this evolving system, taken with the instrument's dither turned off, was monitored as a function of time, as shown in Fig. 5.

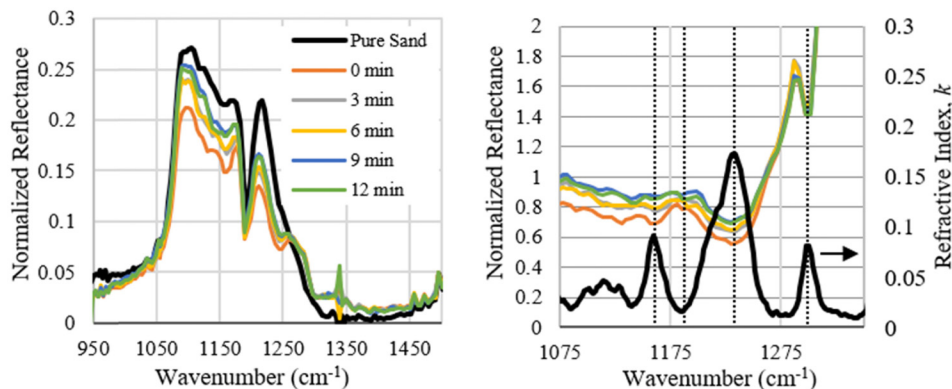


Fig. 5. (left) DRS at increments after deposition of 60 μL of VX onto sand plotted along with the DRS spectrum of sand alone, shown in black. (right) DRS spectra of VX on sand divided by DRS spectrum of sand alone. The black line on right plot is k of VX. The colors indicating time after deposition are the same for both plots.

Crucially, as VX seeped into sand, it appeared to ‘wet’ sand grains. As shown in Fig. 5, the DRS data have an appearance of being dominated by the absorptive component, k , no matter the seepage time allotted. That is, the normalized spectra shown in Fig. 5 show spectral features that are driven by the imaginary part of the index, k : VX reflectance is low where VX absorbs strongly. The morphology of the sample, a thin analyte film coating small sand particles, likely encourages scattering of the light into the film, resulting in the observed absorption-dominated spectral features.

Note also that the seepage of the liquid into the sand is a slow process that appears to be slowing with time. It is interesting to consider for how long detectable VX would persist in this case. Neglecting photolytic activity and chemical reactions and given that the vapor pressure of VX is nearly zero at typical temperatures, we might expect the strong VX/sand affinity to allow for VX to remain detectable on sand long after the initial contamination occurred.

3.2 Droplet Spread

In this section, we focus on the effect of a droplet's physical evolution into a thin film on the surface of a substrate, a process governed by the competition between the surface tension of the analyte versus the affinity it may have for the substrate. Figure 6 shows the time-evolved spectra of 1 μL of VX deposited as a droplet on sandblasted stainless steel, taken with the instrument's dither turned on. At the outset, the 2×2 cm interrogation area of the instrument was certainly overfilling the small droplet's area, and the reflectance is thus dominated by the slightly sloped DRS spectrum (shown in orange) characteristic of the steel substrate used here. As the analyte begins to spread, contribution from steel to the spectrum decreased and hence the resulting spectrum starts to look more like the VX spectrum shown in black. The qualitative appearance of the emerging spectra is best characterized by the calculated air/analyte Fresnel reflection which is overlaid in the plot. This indicates that there was minimal contribution to the spectra from transfectance (transmission through the film and reflection off the substrate) and the spectra were dominated by Fresnel reflection at the air/analyte interface.

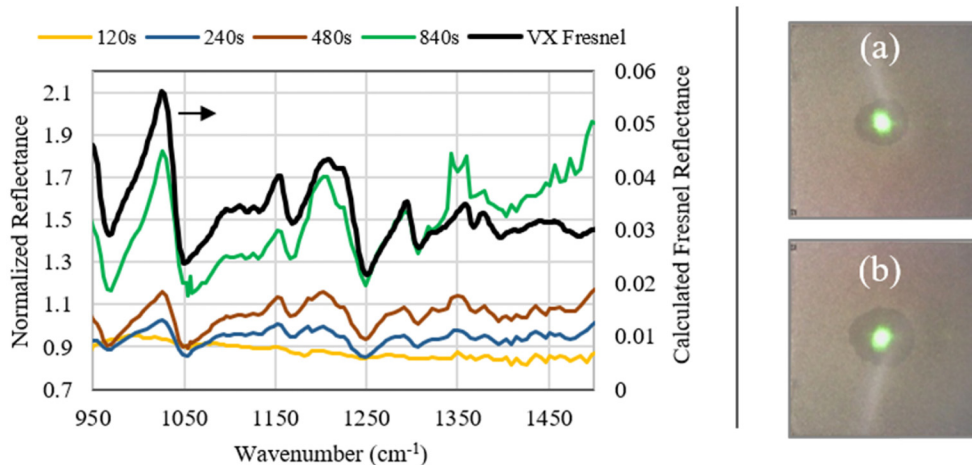


Fig. 6. (left) Time lapse DRS signal from a single 1 μL drop of VX on sandblasted stainless steel. Also shown is the air/analyte interface Fresnel reflectance spectrum of VX. (right) Photographs of the droplet immediately after deposition (a) and 840 sec later (b). The green sighting laser overlapping the combined QCLA outputs has a diameter of 2 mm.

As the roughened stainless steel used here is neither strongly reflecting nor highly structured in its differential reflectance, it is straightforward to uncouple its spectral contribution from that of the analyte. Section 3.3 describes a situation where substrate decoupling is more difficult.

3.3 Variability of Droplet/Substrate Contributions

To illustrate the difficulty introduced by analyte/substrate systems where the substrate is both highly reflecting and possesses strong differential absorption/reflectance and the analyte is highly absorbing, the chemical T-mustard is used. As with VX, we began by centering on a single droplet immediately after deposition, with the dither turned off. Images of T-mustard droplets deposited on glass and stainless-steel substrates are shown in Fig. 7, which again illustrates analyte presentation on different substrates. The DRS spectrum of a single 15 μL droplet on glass is also presented as the blue trace in Fig. 7. Contrary to VX on steel, this droplet's reflectance is governed by the imaginary part of the refractive index. By activating the dither for a typical 2×2 cm areal sweep, the contribution from glass (shown as the green trace in Fig. 7) easily dominates that of T-mustard in magnitude, making the two hard to

uncouple. In this case, the dithered laser beam spends a sizable portion of the measuring time interrogating the glass substrate only, whose reflectance is mostly specular, well captured by the instrument at normal incidence. The specularity of the reflection on glass, coupled with the normal incidence configuration, explains the large amplitude of the glass signature, compared, for example, with the diffuse reflectance obtained on rough substrates such as sandblasted aluminum or steel. In the case of T-mustard on glass, there was very little spread, even over the course of several hours. The viscosity and surface tension of T-mustard dominate the affinity it has for borosilicate glass, so it was not possible to form a uniform film, even by using a pipette tip to deliberately spread the material. The size of the droplets corresponds to a small curvature radius at air/analyte interface and thus results in poor collection efficiency of the highly divergent Fresnel reflection for all alignments. Also, the droplet acts as a quasi-hemispheric lens for the light that is transmitted through the air/analyte interface, focusing close to the analyte/glass interface. Such configuration could explain the large k -dominated signal obtained for the glass substrate case with no dither. In fact, signal was only obtained after careful alignment of the laser to the droplet, indicating strong position dependence.

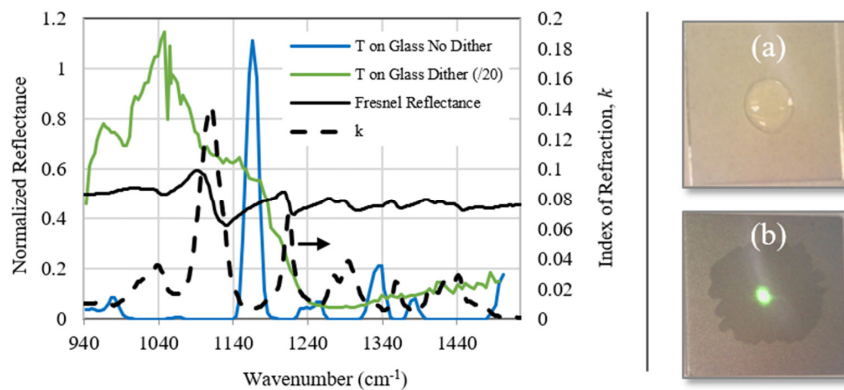


Fig. 7. (left) Standoff spectrum of a single 15 μL drop of T-mustard deposited onto borosilicate glass obtained at 1.3 m standoff. Dither is turned off such that the beam hits the apex of the hemisphere (blue) and then turned on such that the system is scanning around and through the small droplet, spending most of the time on glass (green). (right) Photographs of the droplet immediately after deposition on borosilicate glass (a) and on roughened stainless steel (b).

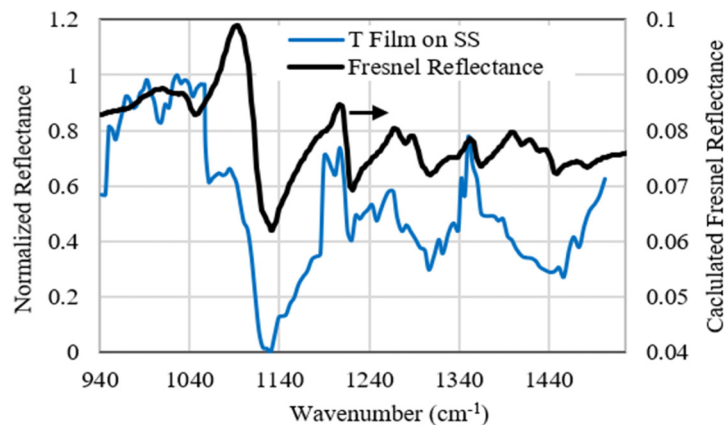


Fig. 8. Spectrum obtained from a single 15 μL drop of T-mustard after spreading the drop into a thin film on roughened stainless steel (Pictured in Fig. 7(b)).

Finally, to examine the effect of the droplet morphology, we deposited an identical 15 μL aliquot of the material on the same stainless type that had been used for VX in the previous section. On roughened steel, the T-mustard did wet the substrate (see photograph in Fig. 7(b)) with the aid of some gentle manipulation using a pipette tip. Figure 8 shows the DRS result of this pairing with the dither turned on. The reflectance signature measured is now more consistent with a Fresnel reflection at the air/analyte interface. The large viscosity of T-mustard results in a smooth air/analyte interface, strengthening this reflection component, while the k-dominated component undergoes reflection on the rough sandblasted stainless steel and is thus more diffuse and less efficiently captured by the limited aperture of the telescope.

We emphasize that such considerations are broad strokes to explain the overall aspect of the measured spectrum, and not a detailed model. As noted by others [15], the DRS spectra from films are strongly affected by slight changes in film thickness, substrate roughness, and substrate reflectivity. To complicate matters, camera images obtained during this work show that for films of highly viscous materials such as T-mustard, the film is non-uniformly thick and does not always appear as a smooth plane at the air/analyte interface.

4. Conclusions

As the physical presentation of a given liquid/substrate combination evolves, so too does its DRS spectrum. As prior knowledge of the most influential DRS factors is generally not available to the user in a standoff situation, a fully integrated instrument would benefit from a decision tree that engages both standard comparison libraries and the ability to model significant variations from these libraries based on the physical data for the chemicals and substrates of interest. Ideally, such an instrument would also be able to *locate* small droplets or crystals within an area that is only partially covered with droplets and/or particles. For instance, the present system utilizes dithering of the QCLA beam only to mitigate speckle. Future work will expand the role of the dither optics such that they work with the computational system to first survey a rectangular frame, locate condensed phase chemicals within that frame, and then direct the interrogation laser toward the droplets or crystals for targeted analysis. The authors are presently developing this location ability and the related ability to perform hyperspectral imaging.

Funding

This work was supported by funding from: The Defense Threat Reduction Agency (HDTRA1-12-C-0099), the US Army (A14A-015-0053) the UK Ministry of Defense (CBRN/00208B), and the Department of Homeland Security, Science and Technology Directorate, Homeland Security Advanced Research Projects Agency (HSQDC-12-C-00067).